A compact 2D matrix array comprised of hexagonal transducer elements for fast volumetric ultrasound imaging

Favre, Hugues; Berendsen, Merijn; Waasdorp, Rick; Maresca, David

Citation (APA)
Favre, H., Berendsen, M., Waasdorp, R., & Maresca, D. (in press). A compact 2D matrix array comprised of hexagonal transducer elements for fast volumetric ultrasound imaging. *IEEE Transactions on Ultrasonics, Ferroelectrics, and Frequency Control*, *72*(9), 1272-1281. https://doi.org/10.1109/TUFFC.2025.3591315

Important note
To cite this publication, please use the final published version (if applicable).
Please check the document version above.

A Compact 2-D Matrix Array Comprised of Hexagonal Transducer Elements for Fast Volumetric Ultrasound Imaging

Hugues Favre, Merijn Berendsen, Rick Waasdorp, and David Maresca

Abstract—**Advances in 4-D ultrasound imaging open new perspectives in biomedical research by reducing the long-standing challenge of operator dependency. Extensive research efforts are focused on developing next generation of 2-D transducer arrays for 4-D imaging. Here, we present a compact 2-D array design based on hexagonal-shaped transducer elements. We demonstrate that 2-D hexagonal arrays provide an optimal compact sampling, resulting in lower grating lobe levels and an improved imaging quality compared to conventional square-shaped transducer element arrays. A prototype array made of hexagonal transducer elements is presented, and its characterization is provided, demonstrating its imaging capabilities.**

Index Terms— **3-D ultrasound imaging, compact sampling, grating lobes, hexagonal transducer, ultrafast ultrasound imaging.**
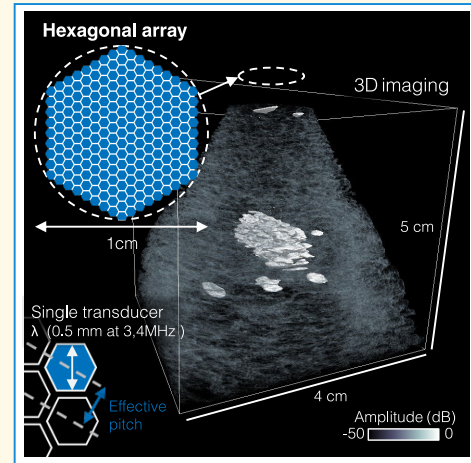
I. INTRODUCTION

ULTRASOUND is one of the most widely used diagnostic tools in clinical practice thanks to its versatility and real-time imaging capabilities [1]. To date, biomedical ultrasound remains predominantly used as a 2-D modality, which makes it prone to intraobserver variability. To address this challenge, there is a need for sensitive transducer arrays supporting fast volumetric ultrasound imaging with an image quality comparable to 2-D ultrasound.

Several 3-D imaging strategies are currently being explored. One approach is to scan a volume of interest with a linear (1-D) array and to stitch data from multiple 2-D planes to form a volumetric image. This can be done by moving a 1-D array mechanically [2], [3], [4] or "free-handed" through accurate position tracking of the linear array or of the imaged

object [5]. Mechanical scanning approaches are efficient and require little additional equipment compared to conventional scanners. A limitation of this approach is that it prevents synchronous data acquisition in space and time, which prevents advanced imaging modes such as 4-D Doppler imaging or 3-D elastography [6].

Another approach is to design 2-D matrix arrays of transducer elements in order to insonify volumes of tissues and sample backscattered echoes in two dimensions. 2-D arrays increase the number of transducer elements, which scales proportionally to the square of the array aperture. Because each transducer element has to be addressed by an electronic channel to form images, 2-D arrays typically display high channel counts that lead to higher manufacturing costs and complexity.

Multiple advances in array design have been reported to maximize the 3-D field of view while limiting element count. Notable examples are sparse array designs [7], multiplexed arrays [8], [9], ultrasound application-specific integrated circuits (ASICs) [10], [11], or row-column-addressed arrays (RCAs) [12]. All of these approaches involve trade-offs in either sensitivity, volume rate, or resolution.

Specific clinical applications, such as cardiac imaging or transcranial imaging, require compact transducer arrays to

Highlights
- **Hexagonal 2-D matrix arrays comprised of hexagonal transducer elements provide a superior imaging performance than square-element arrays.**
- **A 3.4 MHz hexagonal array prototype was manufactured and characterized experimentally.**
- **We report fast volumetric B-Mode imaging with a hexagonal array.**

match the dimensions of intercostal spaces [13] and temporal bone windows [14], [15]. The goal is, therefore, to optimize the packing efficiency of transducer elements across a restricted array surface to ensure optimal wavefront shaping in transmission and spatial sampling of backscattered echoes in reception. Furthermore, the size of individual transducer elements should be maximized to ensure sensitive transmission and reception.

Here, we show that for a given circular array aperture and number of array elements, hexagonal-shaped elements provide a better 3-D imaging performance than square-shaped elements. Note that the fabrication of a hexagonal-element transducer array did not require any additional manufacturing processes, nor did it introduce additional complexity compared to the manufacturing of square-element transducer arrays. Specifically, the hexagonal tiling of a circular array surface reduces grating lobes compared to the square tiling of the same surface. We investigate this geometric transducer element tiling problem in simulation and report the experimental performance of a 3.4 MHz hexagonal 2-D matrix array comprised of 217 hexagonal elements with a circumscribed diameter of 10 mm. This matrix array design was inspired by the primary mirror of the James Webb Space Telescope, which is made up of 18 hexagonal segments [16].

The manuscript is divided into three parts. First, a simulation study that compares two 2-D matrix array designs with circumscribed diameters of 10 mm and comprised of either hexagonal or square transducer elements. Second, a comprehensive hydrophone characterization of a hexagonal array built according to simulated specifications. Third, an experimental investigation of volumetric imaging performance.

II. Materials and Methods

A. Comparison of 2-D Matrix Arrays Comprised of Hexagonal or Square Transducer Elements

1) Geometric Considerations: For this study, we paved a disk with a diameter of 10 mm with either hexagonal or square-shaped transducers as these geometrical shapes enable a compact sampling of the active surface area (in opposition to sparse arrays). The frequency of the array was set to 3.4 MHz, which corresponds to a wavelength (λ) of 0.44 mm in water. The interelement spacing (kerf) was set to 0.1 mm due to manufacturing constraints.

The hexagonal-elements array was made up of 217 hexagons, or 8 concentric rings of hexagons plus a central hexagon, because it is the largest number that can be addressed by a single 256-element ultrasound scanner. The active surface of the hexagonal-element array is 47.0 mm².

TABLE I
ARRAYS SPECIFICATIONS

Quantity	Value for the square element array	Value for the hexagonal element array
Central Frequency	3.4 MHz	3.4 MHz
Bandwidth (-6 dB)	60%	60%
Number of elements	216	217
Element shape	Square	Hexagon
Pitch	0.57 mm (1.3λ)	0.6 mm (1.4λ)
Element width (flat to flat)	0.47 mm	0.5 mm
Element diagonal	0.65 mm	0.58 mm
Kerf	0.1 mm	0.1 mm
Circumscribed aperture diameter	10.0 mm	10.0 mm
Active area	47 mm²	47 mm²

For comparison at equal active surface, we packed the closest possible number of square elements in a disk of equal diameter, which led to a number of 216 square elements (see Fig. 1). The specifications of the two arrays are provided in Table I. The two arrays were modeled with the same simulation setting, which is described in Section II-A2. A hexagonal-element 2-D matrix array was manufactured (Imasonic, Besançon, France) using the exact same specifications as the simulated hexagonal-element array. The prototype array was composed of a backing material, copper electrodes, composite piezoelectric (PZT 1–3), and a quarter-wavelength front end to ensure impedance matching with biological tissue.

2) Volumetric Imaging Simulations: Ultrasound pressure fields and imaging simulations were performed in MATLAB using Field II [17], [18]. Field II simulations compute wave propagation analytically, and transducer elements are modeled under an infinite rigid baffle assumption, which corresponds to an ideal transducer element, free of crosstalk between transducer elements. Ultrasound wave propagation was simulated in homogenous water mimicking medium with a sound speed of 1480 m/s and a linear absorption coefficient of 2.5×10^{-3} dB/cm/MHz.

Square and hexagonal transducer elements were modeled out of smaller square mathematical elements of 17×17 μm² ($\lambda/26$). The simulated transducer material was a common resonant piezoelectric ceramics of 3.4 MHz central frequency and a bandwidth of 60%.

Images were beamformed from simulated pulse-echo radio frequency (RF) data. For the point spread function (PSF) simulation, a point scatterer was positioned at a depth of 35 mm, aligned with the center element of each array. Unsteered plane wave transmissions were simulated (0° angle with respect to
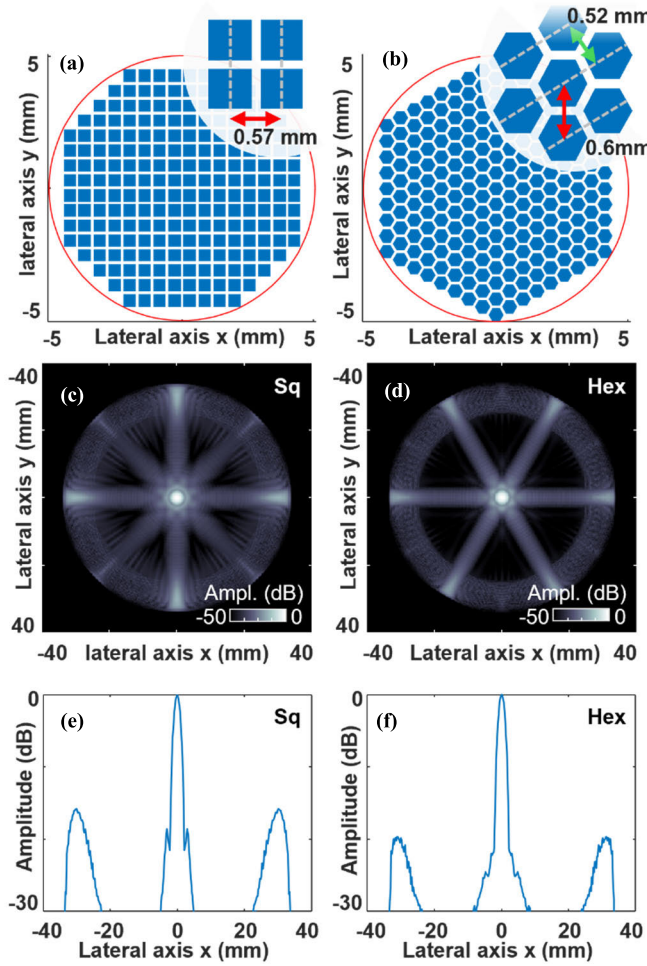
Fig. 1.   PSF comparison between squared and hexagonal transducer array. (a) Design of the square-element transducer array. (b) Design of the hexagonal-element transducer array. Red arrows represent the pitch of each array, while the green arrow represents the effective pitch of the hexagonal array or spatial sampling period. PSF maximum projection on the axial axis z for (c) square-element and (d) the hexagonal-element array. (e) Amplitude profile [...] for the square-element array and (f) the hexagonal array.
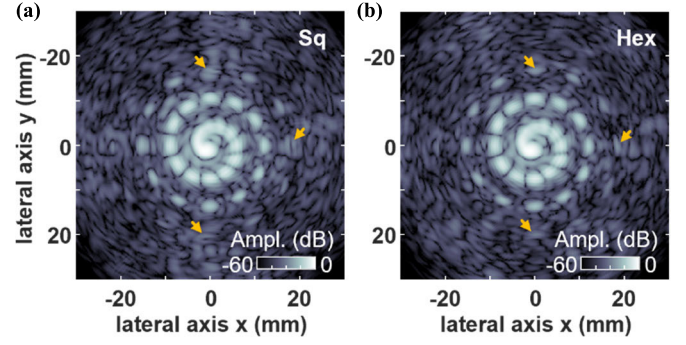

Fig. 2.   Simulated images of point scatterers arranged in a spiral. (a) C-scan at a depth of 35 mm acquired with a square-element array and a single diverging wave transmission. (b) C-scan at a depth of 35 mm acquired with a hexagonal-element array and a single diverging wave transmission. Arrows indicate the position of three point scatterers located on the outer edge of the spiral.

The sampling frequence of the RF data was set to 68 MHz for simulation stability. Conventional delay and sum (DAS) beamforming was performed and images were reconstructed with an isotropic pixel or voxel size of $\lambda/2$.

B. Hydrophone Measurements

To characterize acoustic pressure fields generated by the hexagonal array experimentally, we conducted a series of hydrophone water tank experiments. Our methodology and experimental settings are described below.

1) Experimental Setup and Settings: The probe was controlled using a mid-frequency Vantage-256 scanner (Verasonics, Kirkland, WA, USA). The pressure fields were measured with a 200-μm-diameter polyvinylidene needle hydrophone (model NH0200, Precision Acoustics, Dorchester, U.K.) with a 55 mV/MPa sensitivity, an 8% measurement uncertainty, and a 500-μm-diameter metallic outer shell. The voltage measurements were converted to pressures in accordance to the manufacturer calibration sheet.

The experiments consisted in a series of planar scans, either parallel (B-scan) or perpendicular (C-scan) to the depth axis facing the array. The transmitted ultrasound excitation was a 1-cycle long waveform with a 3.4 MHz frequency and a 67% duty cycle.

2) Transmitted Pressure Fields: We studied acoustic pressure fields generated with four different transmission modes.

1) *Unsteered Focused Beam:* With a focal depth of 35 mm. A low driving voltage of 10 V was applied to minimize the strain on the transducer. The signal was averaged 32 times, and a B-scan was acquired in the xz plane. The x-range was from -10 to $+10$ mm and the z-range was from 5 to 50 mm.

2) *Steered Focused Beams:* With a focal distance of 35 mm from the center of the array, and a steered angle of 15° and 25°. The beam is steered in the plane (Oxz) with the referential of the array, where x is the short axis of the hexagonal array an z the depth. The signal was averaged 32 times and the driving voltage was equal to 10 V. A B-scan was acquired in the xz plane with an x-range from -20 to $+20$ mm and a z-range of 5–50 mm.

the array), and pulse echo RF data were simulated. Fig. 2 simulates and compares imaging of point scatterers arranged in a spiral using both arrays. The simulated propagation medium is composed of 2458 points randomly positioned in space that simulate tissue inhomogeneities. The scattering amplitude (Field II definition) of the inhomogeneities follows a standard normal distribution (standard deviation of 1). In addition, 85 point scatterers with a scattering amplitude of 5 were distributed along a spiral every 30°. The spiral was positioned at a depth of 35 mm. The lateral coordinates of the ith point target $[x_i, y_i]$ of the spiral were following:

$$x_i = \left(1 + \frac{\pi}{6} * i\right) * \sin\left(\frac{\pi}{6} * i\right) \tag{1}$$

$$y_i = \left(1 + \frac{\pi}{6} * i\right) * \cos\left(\frac{\pi}{6} * i\right). \tag{2}$$

Pulse-echo RF data were simulated using a single diverging wave transmission using a virtual point source [6] located at -17.5 mm along the axial direction of the arrays.

3) *Unsteered Plane Wave:* A driving voltage of 10 V was applied and the signal was averaged 32 times. A C-scan was acquired at a depth of 35 mm using an identical *x*- and *y*-range from −15 to +15 mm. The C-scan data was back propagated to the probe surface using angular spectrum analytic method [20] to analyse the active probe aperture [see Fig. 3(d)]. The maximum pressure was quantified on the probe surface area at the transmission time.

4) *Single Element Transmission:* With the center element of the hexagonal array. The driving voltage was set to 10 V and received signals were averaged 128 times to increase SNR. A B-scan was acquired in the *xz* plane with an *x*-range from −20 to +20 mm and a *z*-range of 5–40 mm. This measurement was used to calculate the directivity of a single array element.

3) Spatial Sampling and Experimental Alignment: In all hydrophone measurements, the spatial sampling grid had a resolution of 0.5 mm. Experimental pressure fields were linearly interpolated to increase the grid resolution by a factor of two. The matrix array was aligned relative to the hydrophone using a series of C-scans. A plane-wave transmit was used to set the desired axial distance.

4) Crosstalk Assessment: In a large water tank ($L_{\text{tank}} \gg L_{\text{array}}$), we performed a single element transmission with element i of the array while recording RF data on all elements of the array to measure crosstalk between the transmitting element i and all other elements $j \neq i$. This procedure was repeated for all 217 elements. Crosstalk was plotted as a function of the distance from the transmitting element [see Fig. 3(h)].

5) Simulated Pressure Fields: For comparison, we simulated corresponding pressure fields using the Field-II library. Simulation parameters can be found in Section II-A2. Pressure fields were simulated in 2-D planes using a grid spacing of $\lambda/2$ and temporal sampling of 68 MHz. For each pixel, peak pressure was calculated as the maximum pressure over time.

C. Experimental Imaging Study

We conducted two sets of imaging experiments, one to characterize the PSF of our imaging system, and one to test high-framerate volumetric imaging quality. In both cases, we used a 25 V driving voltage while the hexagonal probe was connected to our programmable ultrasound scanner. All transmitted waveforms were 3.4 MHz equalized square pulses with a 67% duty cycle. The temporal RF sampling rate was set to 20 times the central frequency.

1) 3-D PSF in Water: In this first imaging test, we used the hydrophone needle (model NH0200; Precision Acoustics, Dorchester, U.K.) as a point target to analyse the PSF of our imaging system (hexagonal-element array and scanner). The long axis of the hydrophone needle was aligned with the depth axis, and the tip of the hydrophone needle was positioned at a distance of 35 mm from the central array element. The probe was aligned in depth, in the lateral direction, and radially. A single unsteered plane wave transmission was used to acquire a 3-D image of the PSF, and DAS beamforming was

performed for image reconstruction. We implemented a digital time gain compensation (TGC) in postprocessing, assuming a linear attenuation coefficient of 2.5×10^{-3} dB/cm/MHz. 3-D renderings of volumetric data were obtained using Dragonfly (Comet Technologies, Montreal, QC, Canada).

2) 3-D Imaging of a Tissue-Mimicking Phantom: In this second experiment, we imaged an ultrasound phantom (model CIRS-040GSE, Sun Nuclear, Melbourne, FL, USA). The phantom consisted of a tissue-mimicking medium and contained parallel 0.1-mm-diameter nylon monofilament wires. The targeted region also included a hyperechoic 8-mm-diameter cylinder (+15 dB with respect to the tissue-mimicking phantom material) at a depth of 30 mm. The speed of sound reported by the manufacturer was 1540 m/s, and the attenuation coefficient was 0.5 dB/cm/MHz. We used a diverging wave sequence consisting of 13 angled transmissions relying on a virtual point source formalism [6]. Virtual point sources were positioned at a distance of −17.5 mm with respect to the array. The first source was positioned to face the central element of the array, while the remaining 12 point sources were distributed along the three symmetry axes of the hexagonal grid at angles of −5°, −2.5°, +2.5°, and +5° with respect to the depth axis. The pulse repetition frequency after diverging wave compounding was set to 400 Hz. Here as well, the imaging voltage was set to 25 V. Beamformed 3-D data was visualized using Dragonfly (Comet Technologies, Montreal, QC, Canada).

In this experiment, the contrast ratio (CR) was measured according to the following formula:

$$\text{CR} = 20 * \log_{10} \frac{\overline{s_i}}{\overline{s_o}} \qquad (3)$$

where $\overline{s_i}$ is the average of the envelope signal (before tacking log compression) of the image inside the inclusion, and $\overline{s_o}$ is the average of the envelope signal outside the inclusion and measured at the same depth. The CR was measured in a 2-D plane transverse to the cylindrical hyperechoic inclusion.

III. RESULTS

A. Comparison of Simulated 2-D Matrix Arrays

The PSFs of the square-element and hexagonal-element transducer arrays were compared in simulation (Fig. 1). The full width at half the maximum (FWHM) was identical for both arrays and equal to 2.7 mm. A difference occurs when measuring grating lobes: the grating lobes level is −16 dB for square-element array and −20 dB for hexagonal-element array. The peaks of the grating lobes were positioned at ±30.0 mm for the square-element array and ±31.1 mm for the hexagonal-element array. The total energy contained in the grating lobes, measured as the total energy of the 3-D field of view excluding a sphere of 10 mm centered on the main lobe, was 64% higher for the square-element array than for the hexagonal-element array.

Fig. 2 presents a qualitative imaging comparison of differences between the hexagonal-element and square-element arrays. The higher grating lobes in the square-element array lead to an increased background signal. Point targets located on the outer edge of the spiral [see yellow arrows, Fig. 2(a)
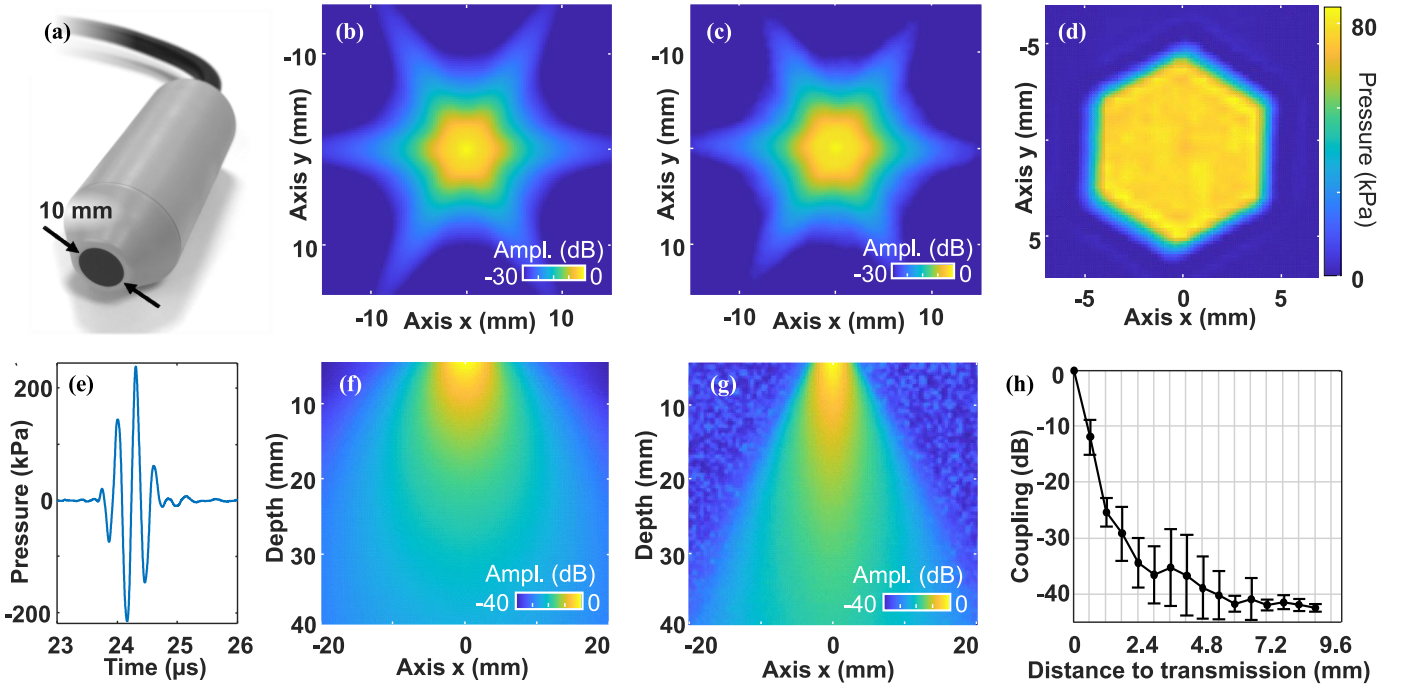
Fig. 3. Hydrophone characterization of the hexagonal-element 2-D transducer array. (a) Photograph of the prototype. (b) Simulated maximum pressure field at 35 mm depth for a plane wave transmssion. (c) Corresponding experimental maximum pressure field. (c) Experimentally measured. (d) Backpropagation of the wave field measured in (c) to the array surface. (e) Temporal response at x, y = 0 and 35 mm depth for the transmit plane wave. (f) Simulated single transducer maximum pressure field. (g) Corresponding experimental maximum pressure field. (h) Coupling effect observed on the elements of the prototype hexagonal transducer array during single-element transmissions, in a free-space water tank.

and (b)] were more clearly detected by the hexagonal-element array.

B. Theoretical Comparison of Spatial Sampling With a Square and Hexagonal Grid

An analysis of the 2-D sampling capabilities of each array can be performed using equivalent line arrays using the projection slice method described by Steinberg [21], Schwartz and Steinberg [22].

The equivalent 1-D aperture is the projection of all element excitations onto a rotation of the x-axis at angle φ in the plane of the array. The focusing pattern of this equivalent array will be the focusing pattern of 2-D array at that particular cut [22]. We call the sampling period of the 2-D array the maximal sampling period of the equivalent line arrays, because this maximal sampling period will generate the highest grating lobes level of the 2-D array. For the hexagonal array, the sampling period L_h lies in the direction of the grating lobes [$\varphi = 30°$ with respect to the x-axis shown in Fig. 1(b)]. The sampling period of the hexagonal array is

$$L_h = \cos(30) * (\text{kerf} + d_h)$$

where kerf is the interelement spacing and d_h, the width of the hexagonal transducer (distance separation of parallel sides). The addition of kerf and d_h is commonly referred as the pitch of the array. Thus, L_h can be seen as the "effective pitch" of the array that generates the grating lobes. For the square-element array, the sampling period L_h is simply the pitch. Numerically, the sampling period is 0.57 mm for

the square-element array and 0.52 mm for the hexagonal-element array. The shorter sampling period of the hexagonal array generates a lower grating lobe level at a wider angle from the main lobe compared to the square array.

This brief comparison can be expanded to other frequencies or surface areas. If we neglect the border effect, filling a disk of radius R with square transducer elements of width d_s, the number of elements N_s is given by

$$N_s = \frac{\pi R^2}{d_s^2}. \tag{4}$$

If we consider hexagonal shape transducer elements of width d_h (separation distance of parallel sides), the number of hexagons N_h filling the disk is

$$N_h = \frac{2\pi R^2}{\sqrt{3}\, d_h^2}. \tag{5}$$

If the number of elements is constrained to be equal, it leads to the relation

$$d_s = \left(\frac{\sqrt{3}}{2}\right)^{\frac{1}{2}} d_h. \tag{6}$$

Then, if the kerf is neglected, the sampling period relation between the square array and the hexagonal array is given by

$$L_s = \left(\frac{2}{\sqrt{3}}\right)^{\frac{1}{2}} L_h \tag{7}$$

$$L_s \approx 1.07\, L_h. \tag{8}$$

The square-element array has a higher sampling period than the hexagonal-element array by 7%.

C. Hydrophone Characterization of the Hexagonal Array Prototype

The hexagonal-element transducer array, previously modeled in simulation, was manufactured according to simulated specifications, and hydrophone pressure measurements were conducted to assess its performance. A photograph of the prototype (Imasonic, Besançon, France) is displayed in Fig. 3(a). The maximum pressure field for a plane wave transmission was in good agreement with the simulation results Fig. 3(b) and (c). For a 10 V pulse transmission, a peak positive pressure of 239 kPa was measured at 35 mm depth, as shown in the temporal response Fig. 3(e). The pressure measurements from the plane-wave transmit were back-propagated to the surface of the array (depth $z = 0$ mm), revealing the hexagonal shape of the active surface, [see Fig. 3(d)]. The average peak pressure at the surface of the array from the backpropagation experiment is 74 kPa (std of 2 kPa).

Next, we evaluated the beam profile radiated by a single hexagonal element of the array in simulation [see Fig. 3(f)] and experimentally [see Fig. 3(g)]. A clear difference in directivity was observed, the pressure field was more directive for the manufactured prototype. We quantified the angular aperture of both beams and measured an angular aperture of $76°$ in simulation versus a $36°$ angular aperture experimentally. This difference could be explained by the coupling effect occurring in the experimental scenario, and measured in [see Fig. 3(h)]. For single-element transmission, closest neighbor elements displayed a -12 dB crosstalk level on average (std $= 3$ dB, $N = 217$).

D. Focusing Performance

The maximum pressure field for a geometrical focus transmit at 35 mm depth on axis and off axis was simulated and measured experimentally (Fig. 4). We report the cases of an unsteered beam [see Fig. 4(a) and (b)], of a $15°$ angled beam [see Fig. 4(c) and (d)] and of a $25°$ angled beam [see Fig. 4(e) and (f)]. The transverse FWHM of the focus beam, the peak coordinate corresponding to the acoustical focus, and the grating lobe levels are measured for the simulation and experimental cases. The different quantitative measurements are gathered in Table II for the unsteered, $15°$, and $25°$ steered focus beam. Grating lobe level of the $15°$ steered focus beam is measured at -22 dB in the experiment (-21 dB in simulation). The grating lobe level increases to -10 dB in the experiment (-18 dB in simulation) when the focus beam is steered with a $25°$ angle.

E. Volumetric Imaging Study

The 3-D PSF of the imaging system was evaluated by insonifying with a single plane wave transmission the tip of the needle hydrophone positioned at a depth of 35 mm and centered relative to the array [see Fig. 5(a)–(d)]. A 3-D image of the PSF is displayed in Fig. 5(a), the maximum projection of the 3-D PSF along the depth axis is displayed in Fig. 5(b), and the ZX plane is displayed in Fig. 5(c) and the corresponding maximum projection along the depth axis in Fig. 5(d) to highlight the grating lobes levels. The first observation is that
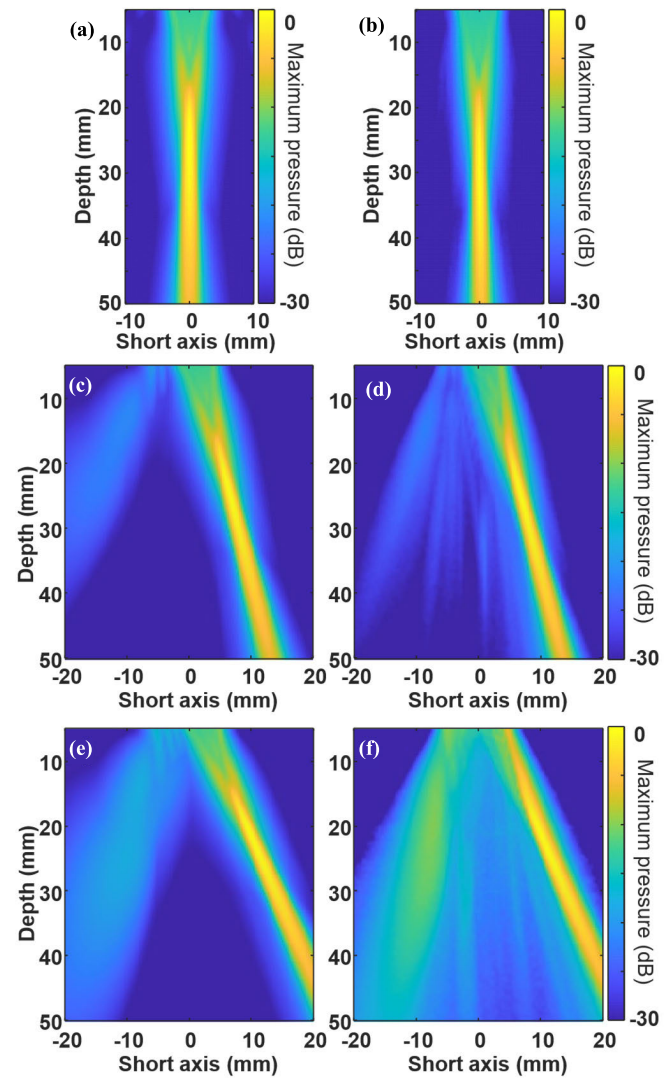

Fig. 4. Comparison of ultrasound focusing with the simulated and prototype hexagonal-element 2-D array. (a) Simulated maximum pressure field focused at a depth of 35 mm in water. (b) Corresponding experimental result. (c) $15°$ angled simulated maximum pressure field focused at a depth of 35 mm. (d) Corresponding experimental result. (e) $25°$ angled simulated maximum pressure field focused at a depth of 35 mm. (f) Corresponding experimental result.

TABLE II
FOCUS BEAM QUANTIFICATION

Metric	Steered angle	Simulation	Experiment	Difference
Trans. FWHM (mm)	0°	2.0	1.9	5 %
	15°	2.4	2.6	6 %
	25°	2.6	2.7	4 %
Peak coord. *[r (mm), θ (°)]*	0°	[26.0, 0.0]	[29.5, 0.0]	[13%, 0 %]
	15°	[24.4, 15.0]	[26.0, 15.2]	[7 %, 1 %]
	25°	[23.9, 25.0]	[24.0, 25.4]	[0 %, 2 %]
Grating lobe level (dB)	15°	- 21	- 22	5 %
	24°	- 18	- 10	44 %

Fig. 5(b) is in good agreement with Fig. 1(d). Experimentally, the grating lobe level of the hexagonal-element 2-D array was
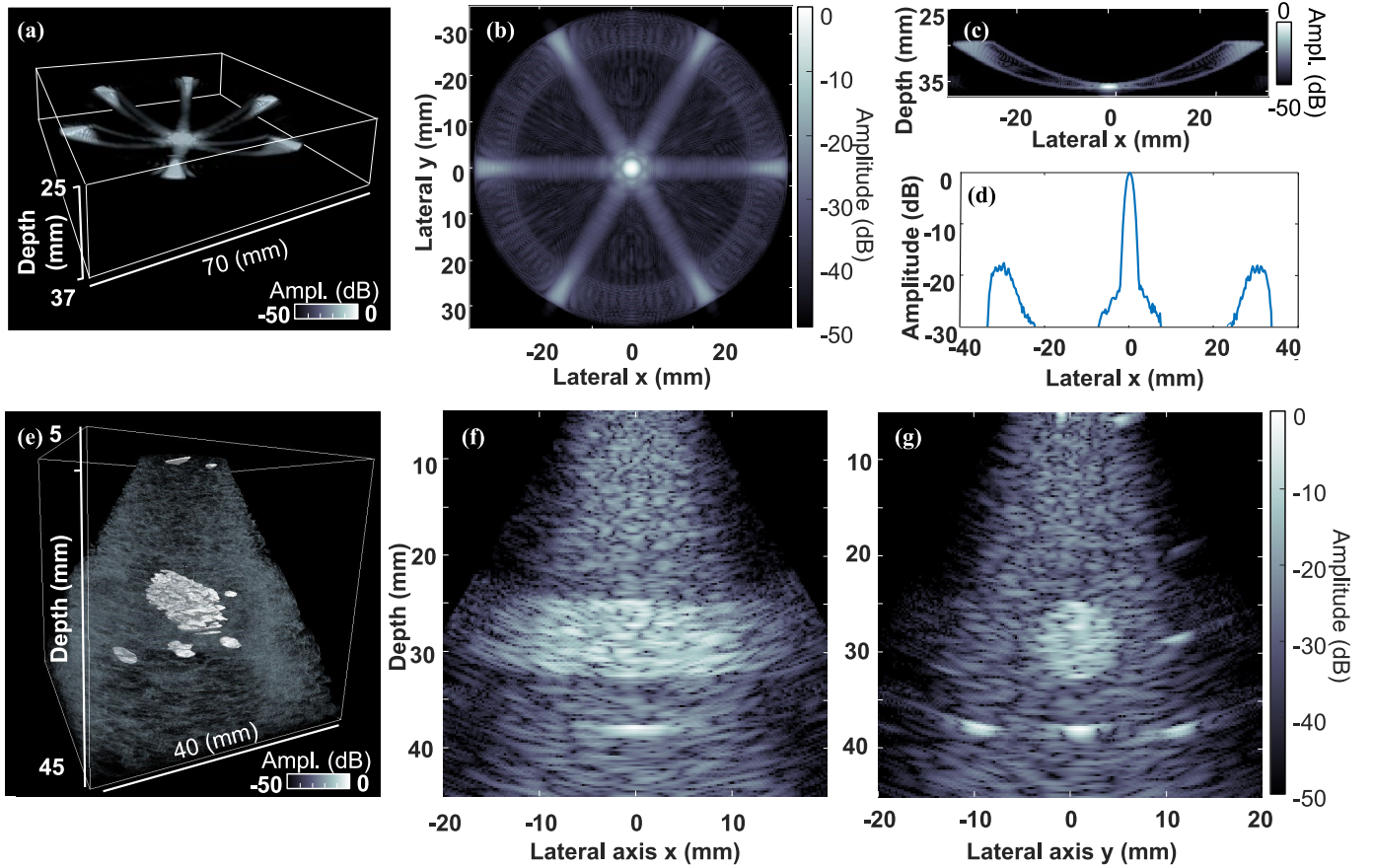
Fig. 5.   Volumetric B-mode images acquired with the hexagonal-element 2-D array prototype. (a) Image of the tip of a needle hydrophone, representing the 3-D PSF of the 2-D array. (b) Maximum projection of the PSF along the depth axis. (c) Cross section of 3-D PSF along the depth and x-axis for $y = 0$. (d) Profile of the maximum projection of the PSF cross section in (c), along the depth axis. (e) Volumetric image of a CIRS phantom acquired with the hexagonal-element 2-D array prototype. (f) Cross section of (e) taken at $y = 2$ mm. (g) Cross section of (e) taken at $x = 0$ mm.

measured at -18 dB and located at ±30 mm in the lateral direction.

Next, we imaged a tissue-mimicking phantom using 13 angled diverging wave [see Fig. 5(e)–(g)]. The CR of the hyperechoic was measured to 15 dB, the FWHM of the 100 μm wire located at $y = 0.8$ mm, $z = 38$ mm was 2.19 mm (or 4.8λ) in the lateral direction and 0.7 mm in the axial direction (or 1.5λ).

IV. DISCUSSION

The idea underlying this study was to tile the circular surface of a 2-D matrix array with hexagonal shaped transducer elements rather than square shaped elements because regular hexagons provide a superior packing efficiency [23]. Using hexagonal elements, we maximize the surface area of individual elements to increase sensitivity in transmit and receive, limit the number of total elements to address the array with a single scanner, and maintain an adequate spatial sampling of ultrasound fields.

We report a simulation study of square and hexagon-shaped transducer elements paving an equal circular array surface of 1 cm diameter. The number of elements of 2-D arrays is a critical parameter affecting image quality as it relates to signal-to-noise ratio and the level of grating lobes. In addition, the

maximum number of elements is constrained by the number of electronic channels available on ultrasound scanners. Our goal was to keep it below 256 in this study, as it is the largest number of channels that can be addressed by a single commercial ultrasound scanner. Since the packing of hexagons in circles follows a mathematical sequence [23], the number of hexagons was set to 217, the largest number below 256.

As the number of elements and the active surface aperture of the arrays were quasi equal, the two 2-D arrays have theoretically the same sensitivity in reception and the same focusing gain and quality. As expected, the PSF comparison of the square-element and hexagonal-element array shows no difference at the focus, Fig. 1.

However, grating lobes affect the contrast of ultrasound images and can lead to artifacts in media with large acoustic impedance mismatches, such as the heart or the bladder.

We showed that the circular tiling of regular hexagons outperforms the circular tiling of squares in terms of maximum grating lobe level (-20 dB for the hexagonal array and -16 dB for the square array). Because of lattice distribution, the hexagonal-element 2-D array exhibits six grating lobes, whereas the square-element 2-D array exhibits a total of eight grating lobes, four grating lobes of first order and four grating lobes of second order. The total energy contained in the grating

lobes was 64% higher in the case of a square-element 2-D array. In addition, the peak pressure of the grating lobes of the hexagonal-element array was spaced 1.1 mm further from the main lobe compared to the square-element array. This can be explained by the sampling period of the arrays [see Fig. 1(b)], which are 0.57 and 0.52 mm for the square-element and hexagonal-element arrays, respectively. A higher sampling period will indeed generate higher grating lobe levels that are closer to the main lobe. Together, these grating lobe considerations are in favor of hexagonal elements. To qualitatively assess the impact of grating lobes, we simulated volumetric imaging of a spiral structure embedded in a scattering medium using a single diverging wave transmission (Fig. 2). The higher grating lobe levels generated by the square-element array lead to an increased background noise and hinder the detection of point scatterers on the rim of the spiral target. In comparison, the hexagonal-element array enabled a sharper detection of these targets.

In addition to the circular aperture arrays compared in simulation, we provide a second case study in the Appendix for rectangular aperture arrays. Here as well, the hexagonal array design provided lower grating lobe levels and reduced energy contained in the grating lobes. Note that we have not explored the impact of the orientation of the square or hexagonal tiling within a given aperture shape, which could be another interesting parameter to optimize.

Our study highlights the concept of "effective pitch" of a 2-D array, building on seminal work by Steinberg [21], Schwartz and Steinberg [22]. Their approach provides a powerful tool for the analysis of grating lobes generated by a 2-D transducer array, as exemplified in the present manuscript.

The sampling theoretical development in Section III-B can be "reversed": if a sampling period is imposed by the application. For example, a phased array with a half-wavelength sampling period can be envisioned for imaging at high angles. Thus, for the same number of elements, the active surface of the hexagonal array will be 15% higher and its aperture 7% higher than the square array. In this case, the higher active surface will result in a better sensitivity and lateral resolution for the hexagonal-element array than the square-element array.

A hexagonal-element 2-D matrix array was manufactured according to simulated specifications, and tested experimentally. The hydrophone measurements showed a higher directivity for the experimental probe compared to the simulated one. This increase in directivity could be expected and is due to the electrical and acoustical crosstalk between hexagonal elements of the array [24]. Because of crosstalk, the effective area of a single element transmission is higher than the surface area of a single element, which leads to a higher directivity. Note that because the pitch between elements is larger for the hexagonal case, the level of crosstalk for the square case would be equal to or higher. This directivity difference can also be explained by the element model in the Field II simulation. It was modeled as a rigid baffle of infinite acoustic impedance; this model is known to lower the directivity compared to the experimental data [25].

In the focusing study, a high grating lobes of −10 dB was measured when tilting the beam by 25°, compared to
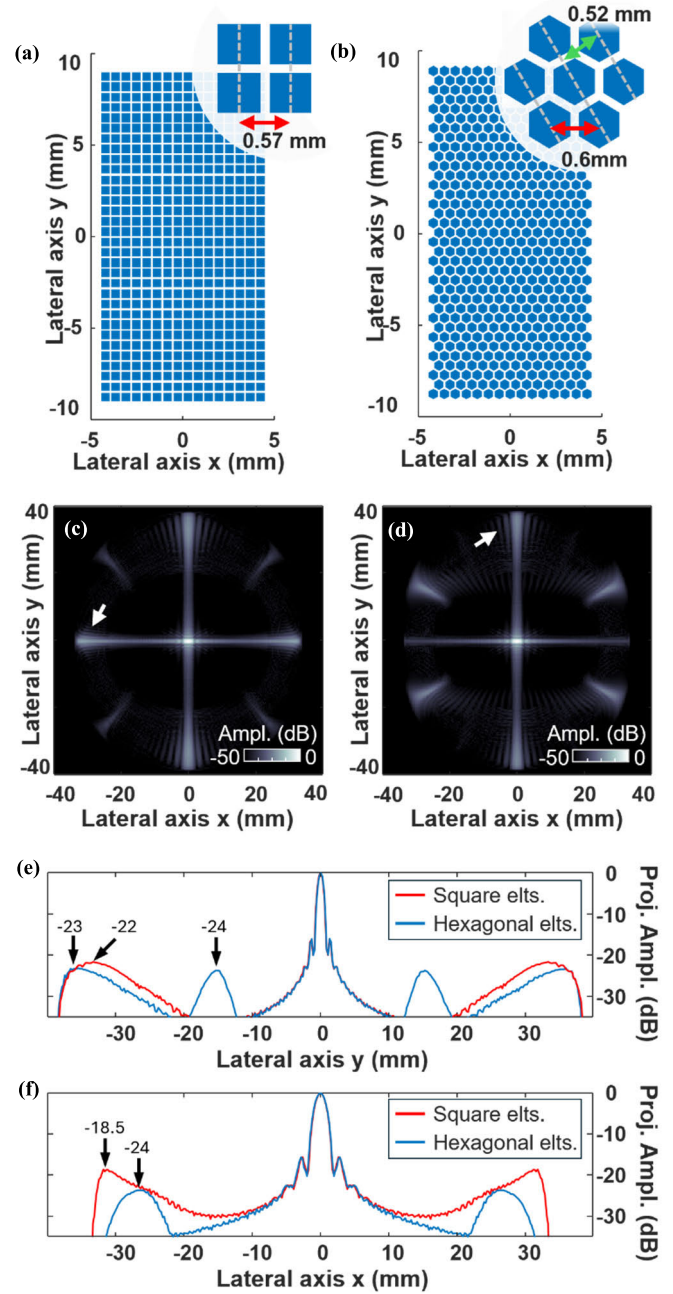

Fig. 6. PSF comparison between a square-element and a hexagonal-element transducer array with rectangular apertures. (a) Design of the square-element transducer array. (b) Design of the hexagonal-element transducer array. Red arrows represent the pitch of each array, while the green arrow represents the effective pitch of the hexagonal array or spatial sampling period. (c) Maximum projection of the PSF on the Oxy plane for the square-element array and (d) hexagonal-element array. Whites arrows represent the highest grating lobes. (e) Maximum projections of the PSF on the y axis and (e) x axis, respectively.

−22 dB for the 15° case. A lower directivity as well as a smaller pitch would improve the ability of the array to image at higher angles. The mismatches observed between simulation and experimental results are due to differences in single-element directivity and possible minor misalignments during data acquisition.

The experimental 3-D PSF image showed similar grating lobes levels compared to the simulated case, with a difference

of 2 dB. Volumetric images of the tissue-mimicking phantom showed that high-framerate imaging performance with the hexagonal prototype was nominal.

In this study, we used 217 elements arranged in concentric hexagonal rings around a central element. As explained previously, this choice was made to keep the total number of electronic channels to address below 256, the maximal number of channels that can be operated by a single ultrasound scanner without multiplexing. Note that in the future, the geometric problem of filling hexagons in a circle, which has no analytical solution, will be further optimized to approach a value of 256 elements.

The manufactured prototype exhibits a high crosstalk level of up to −12 dB, which affects both the field of view and the resolution of the imaging system. In contrast, clinical arrays typically exhibit crosstalk levels below −30 dB. Therefore, further optimization of the manufacturing process regarding element isolation and crosstalk reduction techniques should be considered in future studies [24], [26].

Hexagonal tilling of square transducer elements has already been reported in the past to reduce grating lob levels compared to rectangular tilling [27], [28], but to our knowledge, it is the first time that hexagonal-shaped piezoelectric transducer elements are being used for imaging.

Two-dimensional matrix array design based on hexagonal elements has the potential to improve the performance of advanced 3-D ultrasound imaging methods [7], [29], [30], whether users seek to optimize sensitivity, field of view, or grating lobe levels. Such geometric considerations are beneficial for all transducer technologies, from piezoelectric arrays to pMUTs, CMUTs [31], [32], and wearable arrays [33], [34].

V. Conclusion

This study highlights the advantage of designing 2-D matrix arrays made of hexagonal elements, which provide a compact and efficient spatial sampling solution for 3-D ultrasound imaging. Through simulations and the experimental characterization of an array prototype, we demonstrate that transmission and reception with hexagon grids offer improvements over conventional square-element arrays, particularly by reducing grating lobe levels for a given aperture size and number of transducer elements. The packing efficiency of hexagonal grids also maximizes the active surface area while providing an optimal compact sampling. In summary, hexagonal-element 2-D arrays are especially advantageous when the aperture is constrained by acoustic windows, making it a promising array design for 3-D cardiac imaging or 3-D transtemporal imaging applications.

Appendix

We provide a comparison between 9×18 mm rectangular aperture arrays composed of square or hexagonal elements. This rectangular geometry could be more suitable for certain imaging applications (e.g., intercostal imaging), particularly when a large number of channels is available. The tilling and element size were identical to those reported in

Section II-A1. The square element array had 512 elements and an active surface of 111 cm^2, see Fig. 6(a). The hexagonal element array had 508 elements and an active surface of 110 cm^2, Fig. 6(a). We compared simulated PSFs at a depth of 35 mm following the methodology described in Section II-A2. New Fig. 6(c) and (d) display the maximum intensity projection of the PSF in the *XY* plane for the square element array and hexagonal element array, respectively. New Fig. 6(e) and (f) display the maximum intensity projection of the PSF in the *x*- and *y*-axes, respectively. Highest grating lobe levels are indicated by the white arrows in Fig. 6(c) and (d). The hexagonal array exhibited a lower grating lobe level than the square array (−18.5 and −23 dB for the square and hexagonal element arrays, respectively). The energy contained in the grating lobes was 44% higher for the square-element array.

Author Contributions

Hugues Favre and David Maresca: conceived the study; Hugues Favre and Rick Waasdorp: implemented hexagonal grids in Field II for simulation; Merijn Berendsen: acquired experimental data; Hugues Favre and Merijn Berendsen: processed simulated and experimental data; and Hugues Favre, Merijn Berendsen, and David Maresca: wrote the first draft. All authors edited and approved the final version of the manuscript.

References

[1] C. L. Moore and J. A. Copel, "Point-of-care ultrasonography," *New England J. Med.*, vol. 364, no. 8, pp. 749–757, 2011.

[2] A. Fenster, D. B. Downey, and H. N. Cardinal, "Three-dimensional ultrasound imaging," *Phys. Med. Biol.*, vol. 46, no. 5, pp. R67–R99, May 2001, doi: 10.1088/0031-9155/46/5/201.

[3] A. Fenster, G. Parraga, and J. Bax, "Three-dimensional ultrasound scanning," *Interface Focus*, vol. 1, no. 4, pp. 503–519, Jun. 2011, doi: 10.1098/rsfs.2011.0019.

[4] A. Bertolo et al., "High sensitivity mapping of brain-wide functional networks in awake mice using simultaneous multi-slice fUS imaging," *Imag. Neurosci.*, vol. 1, pp. 1–18, Nov. 2023, doi: 10.1162/imag_a_00030.

[5] M. H. Mozaffari and W.-S. Lee, "Freehand 3-D ultrasound imaging: A systematic review," *Ultrasound Med. Biol.*, vol. 43, no. 10, pp. 2099–2124, Oct. 2017, doi: 10.1016/j.ultrasmedbio.2017.06.009.

[6] J. Provost et al., "3D ultrafast ultrasound imaging in vivo," *Phys. Med. Biol.*, vol. 59, no. 19, pp. L1–L13, Oct. 2014, doi: 10.1088/0031-9155/59/19/l1.

[7] A. Ramalli, E. Boni, E. Roux, H. Liebgott, and P. Tortoli, "Design, implementation, and medical applications of 2-D ultrasound sparse arrays," *IEEE Trans. Ultrason., Ferroelectr., Freq. Control*, vol. 69, no. 10, pp. 2739–2755, Oct. 2022, doi: 10.1109/TUFFC.2022.3162419.

[8] B. Savord and R. Solomon, "Fully sampled matrix transducer for real time 3D ultrasonic imaging," in *Proc. IEEE Symp. Ultrason.*, Oct. 2003, pp. 945–953, doi: 10.1109/ULTSYM.2003.1293556.

[9] J. Yu, H. Yoon, Y. M. Khalifa, and S. Y. Emelianov, "Design of a volumetric imaging sequence using a vantage-256 ultrasound research platform multiplexed with a 1024-element fully sampled matrix array," *IEEE Trans. Ultrason., Ferroelectr., Freq. Control*, vol. 67, no. 2, pp. 248–257, Feb. 2020, doi: 10.1109/TUFFC.2019.2942557.

[10] C. Chen et al., "A front-end ASIC with receive sub-array beamforming integrated with a 32×32 PZT matrix transducer for 3-D transesophageal echocardiography," *IEEE J. Solid-State Circuits*, vol. 52, no. 4, pp. 994–1006, Apr. 2017, doi: 10.1109/JSSC.2016.2638433.

[11] D. S. Dos Santos et al., "An ultrasound matrix transducer for high-frame-rate 3-D intra-cardiac echocardiography," *Ultrasound Med. Biol.*, vol. 50, no. 2, pp. 285–294, Feb. 2024, doi: 10.1016/j.ultrasmedbio.2023.11.001.

[12] J. A. Jensen et al., "Three-dimensional super-resolution imaging using a row–column array," *IEEE Trans. Ultrason., Ferroelectr., Freq. Control*, vol. 67, no. 3, pp. 538–546, Mar. 2020, doi: 10.1109/TUFFC.2019.2948563.

[13] I. Aly et al., "Cardiac ultrasound: An anatomical and clinical review," *Transl. Res. Anatomy*, vol. 22, Jan. 2021, Art. no. 100083, doi: 10.1016/j.tria.2020.100083.

[14] S. Purkayastha and F. Sorond, "Transcranial Doppler ultrasound: Technique and application," *Seminars Neurol.*, vol. 32, no. 4, pp. 411–420, Jan. 2013, doi: 10.1055/s-0032-1331812.

[15] C. Demené et al., "Transcranial ultrafast ultrasound localization microscopy of brain vasculature in patients," *Nature Biomed. Eng.*, vol. 5, no. 3, pp. 219–228, Mar. 2021, doi: 10.1038/s41551-021-00697-x.

[16] M. W. McElwain et al., "The James Webb space telescope mission: Optical telescope element design, development, and performance," *Publications Astronomical Soc. Pacific*, vol. 135, no. 1047, May 2023, Art. no. 058001, doi: 10.1088/1538-3873/acada0.

[17] J. A. Jensen and N. B. Svendsen, "Calculation of pressure fields from arbitrarily shaped, apodized, and excited ultrasound transducers," *IEEE Trans. Ultrason., Ferroelectr., Freq. Control*, vol. 39, no. 2, pp. 262–267, Mar. 1992, doi: 10.1109/58.139123.

[18] J. A. Jensen, "FIELD: A program for simulating ultrasound systems," in *Proc. IEEE 10th Nordic-Baltic Conf. Biomed. Imag.*, vol. 34, Mar. 1996, pp. 351–353.

[19] J. A. Jensen, S. I. Nikolov, K. L. Gammelmark, and M. H. Pedersen, "Synthetic aperture ultrasound imaging," *Ultrasonics*, vol. 44, pp. e5–e15, Dec. 2006, doi: 10.1016/j.ultras.2006.07.017.

[20] D. Andrés, A. Carrión, F. Camarena, and N. Jiménez, "Methods to design and evaluate transcranial ultrasonic lenses using acoustic holography," *Phys. Rev. Appl.*, vol. 20, no. 4, Oct. 2023, Art. no. 044071, doi: 10.1103/physrevapplied.20.044071.

[21] B. D. Steinberg. *Principles of Aperture and Array System Design: Including Random and Adaptive Arrays*. Accessed: Dec. 6, 2024. [Online]. Available: https://ui.adsabs.harvard.edu/abs/1976wi.book.S

[22] J. L. Schwartz and B. D. Steinberg, "Ultrasparse, ultrawideband arrays," *IEEE Trans. Ultrason., Ferroelectr., Freq. Control*, vol. 45, no. 2, pp. 376–393, Mar. 1998, doi: 10.1109/58.660149.

[23] M. Prvan, J. Ožegović, and A. B. Mišura, "On calculating the packing efficiency for embedding hexagonal and dodecagonal sensors in a circular container," *Math. Problems Eng.*, vol. 2019, no. 1, Jan. 2019, Art. no. 9624751, doi: 10.1155/2019/9624751.

[24] S. Zhou, G. L. Wojcik, and J. A. Hossack, "An approach for reducing adjacent element crosstalk in ultrasound arrays," *IEEE Trans. Ultrason., Ferroelectr., Freq. Control*, vol. 50, no. 12, pp. 1752–1761, Dec. 2003, doi: 10.1109/TUFFC.2003.1256316.

[25] P. Pesque and M. Fink, "Effect of the planar baffle impedance in acoustic radiation of a phased array element theory and experimentation," in *Proc. IEEE Ultrason. Symp.*, Nov. 1984, pp. 1034–1038, doi: 10.1109/ULTSYM.1984.198462.

[26] S. Zhou and J. A. Hossack, "Reducing inter-element acoustic crosstalk in capacitive micromachined ultrasound transducers," *IEEE Trans. Ultrason., Ferroelectr., Freq. Control*, vol. 54, no. 6, pp. 1217–1228, Jun. 2007, doi: 10.1109/TUFFC.2007.375.

[27] M. Pernot, J.-F. Aubry, M. Tanter, J.-L. Thomas, and M. Fink, "High power transcranial beam steering for ultrasonic brain therapy," *Phys. Med. Biol.*, vol. 48, no. 16, pp. 2577–2589, Aug. 2003, doi: 10.1088/0031-9155/48/16/301.

[28] H. Favre, M. Pernot, M. Tanter, and C. Papadacci, "Transcranial 3D ultrasound localization microscopy using a large element matrix array with a multi-lens diffracting layer: An in vitro study," *Phys. Med. Biol.*, vol. 68, no. 7, Apr. 2023, Art. no. 075003, doi: 10.1088/1361-6560/acbde3.

[29] E. Roux, F. Varray, L. Petrusca, C. Cachard, P. Tortoli, and H. Liebgott, "Experimental 3-D ultrasound imaging with 2-D sparse arrays using focused and diverging waves," *Sci. Rep.*, vol. 8, no. 1, p. 9108, Jun. 2018, doi: 10.1038/s41598-018-27490-2.

[30] H. Favre, M. Pernot, M. Tanter, and C. Papadacci, "Boosting transducer matrix sensitivity for 3D large field ultrasound localization microscopy using a multi-lens diffracting layer: A simulation study," *Phys. Med. Biol.*, vol. 67, no. 8, Apr. 2022, Art. no. 085009, doi: 10.1088/1361-6560/ac5f72.

[31] R. Sharma, R. Agarwal, A. K. Dubey, and A. Arora, "Analytical modelling of hexagonal shaped capacitive micromachined ultrasonic transducer," *Int. J. Syst. Assurance Eng. Manage.*, vol. 12, no. 2, pp. 252–262, Apr. 2021, doi: 10.1007/s13198-020-01046-y.

[32] Y. He, H. Wan, X. Jiang, and C. Peng, "Piezoelectric micromachined ultrasound transducer technology: Recent advances and applications," *Biosensors*, vol. 13, no. 1, p. 55, Dec. 2022, doi: 10.3390/bios13010055.

[33] H. Hu et al., "A wearable cardiac ultrasound imager," *Nature*, vol. 613, no. 7945, pp. 667–675, Jan. 2023, doi: 10.1038/s41586-022-05498-z.

[34] S. Zhou et al., "Transcranial volumetric imaging using a conformal ultrasound patch," *Nature*, vol. 629, no. 8013, pp. 810–818, May 2024, doi: 10.1038/s41586-024-07381-5.